A scalable and surfactant-free emulsion method

for producing microbeads from varied biomass

feedstocks

Benjamin P. Robertson, *Audrey J. Miller, *Gerald E. Rott, *Siena Marie

Quinn,[‡] Ehsanur Rahman,[¶] Hannah R. Bachmann,[†] Abbie F. Nistler,[§] Boya

Xiong. and Michelle A. Calabrese*,†

†Department of Chemical Engineering & Materials Science, University of Minnesota,

Minneapolis, MN, 55455, USA

‡Department of Chemistry and Biochemistry, University of California San Diego, La Jolla, CA,

92093, USA

¶Department of Civil, Environmental, & Geo-Engineering, University of Minnesota, Minneapolis,

MN. 55455, USA

§Department of Chemical Engineering, University of Utah, Salt Lake City, UT, 84112, USA

E-mail: mcalab@umn.edu

Phone: +1 612 625 2551

Abstract

Despite national and international regulations, plastic microbeads are still widely used in

personal care and consumer products (PCCPs). These exfoliants and rheological modifiers

cause significant microplastic pollution in natural aquatic environments. Microbeads from

nonderivatized biomass like cellulose and lignin can offer a sustainable alternative to these

non-degradable microplastics, but processing this biomass into microbeads is challenging due

1

to limited viable solvents and high biomass solution viscosities. To produce biomass microbeads of the appropriate size range for PCCPs (~200-800 µm diameter) with comparable shapes and mechanical properties to commercial plastic microbeads, we used a surfactant-free emulsion/precipitation method, mixing biomass solutions in 1-ethyl-3-methylimidazolium acetate (EMImAc) with various oils and precipitating with ethanol. While yield of microbeads within the target size range highly depends on purification conditions, optimized protocols led to >90% yield of cellulose microbeads. Kraft lignin was then successfully incorporated into beads at up to 20% wt; however, higher lignin contents result in emulsion destabilization unless surfactant is added. Finally, the microbead shape and surface morphology can be tuned using oils of varying viscosities and interfacial tensions. Dripping measurements and pendant drop tensiometry confirmed that the higher affinity of cellulose for certain oil/IL interfaces largely controlled the observed surface morphology. This work thus outlines how biomass composition, oil viscosity, and interfacial properties can be altered to produce more sustainable microbeads for use in PCCPs, which have desirable mechanical properties and can be produced over a wide range of shapes and surface morphologies.

Keywords: lignin, cellulose, biomass, microbeads, emulsion, oil, sustainability, degradable polymer

Introduction

Non-degradable plastic microparticles are a significant environmental threat. Due to their small sizes (between 1 µm and 5 mm diameter), ¹ microplastics are particularly difficult to recover from the environment and are prone to circulation throughout the water cycle, atmosphere, and biosphere. Microplastic particles causing inflammatory and carcinogenic effects have been found in tap water, ² in the air, ³ and even in human blood. ⁴ These microplastic particles can be classified as primary – produced at small size scales for use in consumer products like toothpaste or facial scrubs – or secondary, where the small particle size is created by weathering and fragmentation from larger objects like tires or clothes. Estimates of primary, non-degradable microplastic emissions range from ~3 trillion particles per year in the US⁵ to >200 trillion particles per year in

China.6

Although many countries have implemented regulations against using non-degradable plastic microbeads in consumer products, these regulations are not comprehensive. Accordingly, plastic microbeads are still widely used, and few sustainable alternatives with comparable properties exist. Microbeads act as both rheological modifiers and gentle exfoliants in personal care consumer products (PCCPs) due to their defined shape and durable mechanical properties. Thus to effectively replace commodity plastics like polypropylene and polyethylene, degradable alternatives to plastic microbeads should have similar mechanical properties, shapes, and sizes. Commodity plastics typically have Young's moduli of ~1 GPa, and microbeads in consumer products range from tens of microns to over a millimeter. However, particles smaller than ~200 μm are more difficult to capture by sedimentation and sieving in wastewater treatment. Therefore to create more sustainable PCCPs, degradable microbeads with diameters between 200 and 800 μm would provide a target range that is both large enough to be captured during wastewater treatment.

Beyond size, microbead morphology and stiffness critically impact function in PCCPs and other applications. ^{17,18} A tunable surface morphology or a controlled degree of surface roughness is often desirable for PCCP applications, where many plastic microbeads are designed with somewhat irregular shapes and surface morphologies to provide better scrubbing capabilities. ^{10,11,19,20} For example in facial scrubs, ^{11,19} these plastic particles often contain smooth protrusions that can enhance exfoliation without causing damage to the skin. Conversely, microparticles in toothpastes may be rougher and more granular. ²⁰ While natural alternatives like nut shells, seeds, or pumice can provide exfoliation, these alternatives often have sharp, irregular edges and lack the predictable rheological properties of plastic microbeads. ^{21,22} Additionally, these products can cause microabrasions due to the sharp edges, causing damage to the skin if regularly used. ^{18,23} Thus to effectively compete with and replace commercial microbeads, sustainable alternatives should ideally be able to be processed into multiple morphologies for different applications. ¹⁹

An ideal degradable alternative to commodity plastics in PCCPs is lignocellulosic biomass,

which is nearly omnipresent, ²⁴ benign, and commonly used as a biodegradability standard. ²⁵ Nanospheres have been made from cellulose or lignin – a common waste product from isolating cellulose for use in paper and pharmaceuticals. Cellulose nanospheres are created by hydrolysis, ²⁶ mechanical agitation, ²⁷ or precipitation methods, ²⁸ although these are often aggregated into larger structures. Lignin nanospheres have also been produced by precipitation ²⁹ and incorporated into cellulose structures to enhance their resistance to enzymatic hydrolysis. ³⁰ Unfortunately, these biomass nanospheres are too small (<1 µm diameter) to use in PCCPs.

Biomass microbeads of the appropriate size scale for PCCPs (~200 – 800 μm diameter) have also been produced, but current technologies face several challenges. Many of these microbeads require covalent crosslinking ^{9,31} to achieve suitable mechanical properties, or rely on derivatized cellulose for processing – inhibiting degradation and making them prone to regulation. ^{32–34} Other forms of biomass, such as crustacean-derived chitin, ³⁵ contain common allergens ^{36,37}; more processable biopolymers like alginate yield microbeads with low moduli unsuitable for PCCPs. ^{38,39} Unfortunately, nonderivatized, allergen-free biomass like cellulose and lignin that can produce stiff materials is difficult to process. For example, these sources are soluble in limited solvents and upon dissolution, the resulting biomass solutions have high viscosities. ^{40,41} Our recent work addressed a number of these challenges by using a dripping and precipitation method to produce biomass microbeads from nonderivatized cellulose and Kraft lignin feedstocks. ⁴² This process produced spherical microbeads with mechanical properties suitable for PCCPs without requiring covalent crosslinking. These larger beads (>800 μm diameter) were easy to characterize and provided information on how compositional and processing parameters influence bead size, shape, and modulus; however, beads of <800 μm diameter were not accessible and the process had limited scalability. ⁴²

Using emulsion processes – which are widely used in industry to produce polymeric particles ⁴³ – could address both the bead size and limited scalability of the dripping process. Previously, Jo, Park, and coworkers produced magnetic cellulose hydrogel beads using an emulsion method with oil, an ionic liquid (IL) solvent, and surfactant. ^{44,45} While this method was fairly robust to process conditions such as stir speed and temperature, the resulting soft, swollen hydrogel beads were ideal

for enzyme immobilization, but substantially differed from the hard and dense beads needed for exfoliation or scrubbing. ¹⁷ This method also had several drawbacks with respect to consumer and environmental safety: (1) residual IL remained in the beads despite several solvent washes, and (2) surfactants were required, which are typically hard to remove and can hinder biodegradability.

Here for the first time, we demonstrate a scalable emulsion and precipitation process for producing microbeads from mixed feedstocks of purely native, nonderivatized biomass, using oil and IL both with and without surfactant. Applying insights from our prior work, ⁴² the process was first refined to minimize bead aggregation upon purification and improve the yield of beads of the appropriate size and mechanical properties for PCCPs. Kraft lignin was then added as a low-cost filler, successfully producing beads with minimal aggregation up to lignin fractions of 20%. Finally, we show that oil type can be used to mediate bead shape and surface morphology, due to differences in the interfacial activity of cellulose. These trials are supported by interfacial tension measurements between the three phases (oil, IL, precipitation solvent) and dripping experiments. This work outlines a scalable approach for producing biomass microbeads that both upcycles waste lignin and eliminates surfactants, yielding microbeads of tunable surface topology for multiple PCCP uses.

Experimental

Materials

Avicel PH-101 (degree of polymerization (DP)=230) cellulose powder (Sigma-Aldrich) and Kraft dealkaline lignin (TCI Chemical) were used as-received. The ionic liquid (IL), 1-ethyl-3-methyl-imidazolium acetate (EMImAc), was purchased from Astatech (95%). Solvents include hexanes (ACS-grade, Fisher), isopropanol (ACS-grade, Fisher), and ethanol (200 proof, Pharmco-Aaper). Oils used as the continuous phase include sunflower oil (Artizen), heavy mineral oil (USP, Fisher), and S600 viscosity standard (Cannon Instruments). Fourier transform infrared spectra of the starting powders and resulting beads are shown in SI.1.

Biomass solution preparation

Biomass solutions were dissolved with a total concentration of 4% wt in EMImAc by stirring at 50 °C for 48 h. Lignin was incorporated as fractions of the total biomass (f_{lignin}) ranging from 0 to 0.67 (1.3% wt cellulose / 2.7% wt lignin). Solutions were kept at room temperature until used for microbead preparation.

Interfacial tensiometry and dripping experiments

To measure interfacial tension, σ , the pendant drop technique was applied. Here, a drop of the denser phase ($\rho_{cell/IL} > \rho_{oil} > \rho_{ethanol}$) was extruded using an 18g flat needle into the less dense phase inside a rectangular transparent container. The droplet was allowed to equilibrate for ~30 mins, before being backlit with a 2600 lumen light source and imaged with a Chronos 1.4 high-speed camera. These images were then analyzed via an ImageJ plugin ⁴⁶ to extract the interfacial tension. For dripping experiments, the same configuration was used, but the drops were extruded to an unstable volume before being allowed to drip. These videos were analyzed in Matlab as in previous work ^{47,48} to extract values of the minimum radius in time, and the extracted radii were normalized to the radius of the needle, R_0 . The statistical significance of differences between average extracted parameters was determined by using two-sample, one-tailed Student's t-tests.

Microbead formation & purification

Beads were synthesized *via* the emulsion-precipitation method, illustrated in Figure 1. Under the standard conditions, 4% wt biomass solutions in IL were stirred with an immiscible oil phase for 2 hours at 40 °C and 250 RPM. This temperature was chosen to minimize side reactions and prevent evaporation of the precipitation solvent. Subsequently, the heat was turned off, and ethanol was added drop-wise at a rate of 2 to 3 drops per second to precipitate beads. The standard ratio for these components was 1:5:20 biomass solution:oil:ethanol by weight. Using oils with varying interfacial tension resulted in beads with a wide range of morphologies. Following precipitation,

beads were washed and filtered by two different methods. In the first method, the emulsion was gravity filtered and the beads were washed with hexanes and ethanol, and in the second method, the oil was drained prior to vacuum filtration and the beads were washed with hexanes and acetone. Following one of these two methods, residual IL was removed from beads using Soxhlet extraction (Figure S7). Small batches for screening purposes were produced in 20 mL scintillation vials using a magnetic stir bar. Larger scale samples were produced in a glass beaker of 8 cm diameter, using an impeller with blade diameter of 6 cm. Unlike previous work, 44,45 this synthetic method did not incorporate surfactant, allowing for ease of separations (Figure S13). Furthermore, the addition of the extraction step allows for greater safety and environmental compatibility of the final product, which residual IL would compromise.

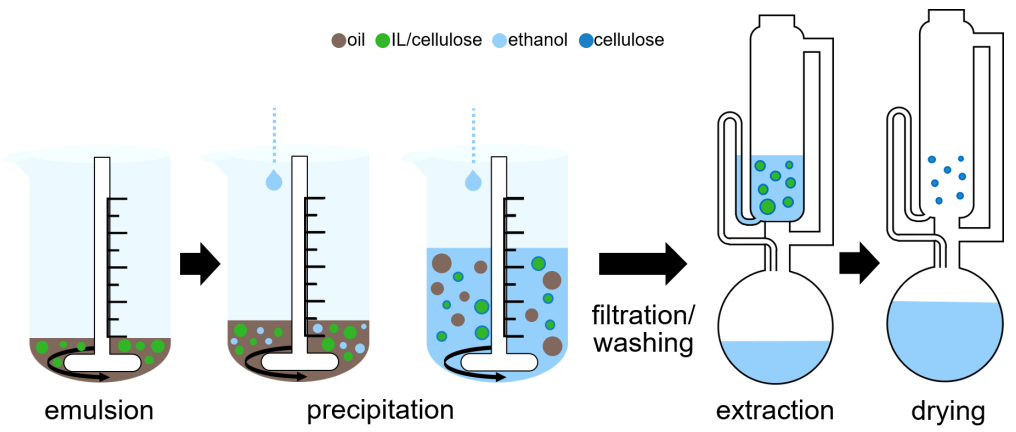


Figure 1: Schematic of biomass microbead preparation and purification procedure. Solutions of biomass in IL were stirred with oil for 2 h to disperse droplets, followed by the addition of ethanol as anti-solvent to precipitate these droplets and form beads. Beads were filtered out and were purified *via* Soxhlet extraction to remove residual solvent.

Microbead size quantification

Beads were spread on paper (black paper for pure cellulose beads, white paper for beads containing lignin in order to maximize contrast) using tweezers for imaging using DAGE-MTI 1920 x 1080 video camera with a Navitar 25 mm varifocal objective lens. Images included a reference of known size for calibration and were sized automatically in ImageJ by thresholding to determine the edges of the samples. Sizing data was down-selected using a minimum area of 0.005 mm² to remove background noise. Bead shapes were fit to ellipses, and diameters D_{bead} were determined based on

the area of each ellipse as $D_{bead} = \sqrt{4A/\pi}$. The aspect ratio of each bead was determined based on the ratio of major to minor axes of these elliptical fits, with a minimum value of 1 corresponding to a perfectly circular bead as viewed from above. Averages and standard deviations were calculated for bead samples with minimum sample size of n=100. To determine yield of beads less than 850 μ m in diameter, bead samples were sieved through a 20 mesh (850 μ m) sieve and weighed. The yield in weight was calculated as the fraction of beads that passed through the sieve, divided by the overall weight of the bead sample. The statistical significance of differences between average measured diameters was determined by using two-sample, one-tailed Student's t-tests.

Atomic force microscopy (AFM)

Nanoindentation experiments were performed by measuring force curves on the beads using an MFP3D-Bio-Atomic Force Microscope (Asylum Research, Santa Barbara, CA). A spherical diamond-like-carbon AFM probe (B2000-v0010-5, NanoAndMore USA Corporation, radius: 2000 μm, spring constant: 32.08 N/m) was used to take force curves at a rate of 0.1 Hz, with the highest applied force of 500 nN. The force curves were fitted to the Johnson-Kendall-Roberts (JKR) model using Igor Pro 3.38B01 software to determine the elastic modulus. The following equations describe the JKR model:⁴⁹

$$a = \left(\frac{R_{eff}}{E_{eff}} (\sqrt{F_{adh}} + \sqrt{F_N + F_{adh}})^2\right)^{1/3}$$
 (1)

$$\delta = \frac{a^2}{R_{eff}} - \frac{4}{3} \sqrt{\frac{aF_{adh}}{R_{eff}E_{eff}}} \tag{2}$$

Here, a and δ represent the contact radius (a) and indentation depth (δ), respectively and they serve as the fitting parameters. F_{adh} is the force of adhesion and F_N describes the normal force at any point. R_{eff} and E_{eff} are the effective radius and effective elastic modulus, respectively, which can be described by $R_{eff} = (1/R_t + 1/R_s)^{-1}$ where R_t and R_s represent the radii of the tip and sample respectively, and $\frac{1}{E_{eff}} = \frac{4}{3}(\frac{1-v_t^2}{E_t} + \frac{1-v_s^2}{E_s})$ where E_t and E_s are the Young's moduli of the tip and

sample and v_t and v_s are the Poisson's ratios of the tip and sample. Here, as the tip was diamond-like-carbon we used the elastic modulus of synthetic diamond for further calculation ($E_t = 865$ GPa and $v_t = 0.2$). ⁵⁰ A value of $v_s = 0.33$ was used for the microbead sample.

Scanning electron microscopy (SEM)

Images of microbead surfaces were obtained using a scanning electron microscope (JEOL JSM-6010PLUS/LA). Microbeads were affixed to an adhesive carbon tape without sputter coating. SEM observations were carried out with secondary electron detector at an acceleration voltage of 2 kV to avoid charging effects, with magnifications from 30x to 850x. Energy-dispersive x-ray spectroscopy (EDS) was performed at an acceleration voltage of 5 kV to ensure sufficient signal (at least 1000 counts per second) for elemental analysis. Based on EDS spectra (which are plotted as normalized by the entire spectrum), IL content was determined based on weight percentage of nitrogen, and lignin content was determined based on weight percentage of sulfur, compared to weight percentage of sulfur present in lignin powder. Bead surface roughness R_q was calculated based on SEM images cropped to include only the bead surface and using the SurfCharJ plugin for ImageJ. 51 R_q is defined as the root mean squared average deviation from the mean grayscale value in the image, and these values were divided by the mean grayscale value to determine $R_{q,norm}$, which was averaged for at least n=5 images. The statistical significance of differences in $R_{q,norm}$ was determined by using two-sample, one-tailed Student's t-tests.

Results and discussion

Development of microbead production process

Beads were synthesized *via* an emulsion-precipitation method, in which 4% wt biomass solutions in ionic liquid (IL) were stirred with an immiscible oil phase to disperse droplets; anti-solvent was subsequently added to precipitate these droplets and form microbeads. Based on previous work screening anti-solvents for a dripping-precipitation method,⁴² ethanol was selected as the anti-

solvent, which is immiscible with all oils examined (SI.2). Unlike other emulsion-precipitation systems – for example aqueous alginate solutions 38 – here, the composition of the continuous oil phase cannot be changed gradually to cause precipitation. Precipitation instead depends on collisions between two phases simultaneously dispersed in oil: ethanol drops and biomass/ionic liquid drops (Figure 1). Dispersion of these drops therefore depends on the applied deformation from stirring overcoming the interfacial tension, σ , and viscosity, η , of the dispersed phase among other factors (Figure S3). Moreover, precipitation of the cellulose/IL solution within the emulsion depends on collisions between ethanol and IL drops. Consequently, the sizes and morphologies of the resulting microbeads should be impacted by a variety of factors, including the interfacial tensions between oil and ionic liquid and between oil and ethanol, the viscosities of all three phases, 52 component ratios, stirring speed, system temperature, and reactor geometry. 38

Small-scale screening trials were first performed in 20 mL scintillation vials and stirred for 2 h to narrow the vast parameter space. Based on prior results employing the dripping-precipitation method, ⁴² cellulose was first dissolved in 70:30 DMSO:EMImAc. While this reduced the viscosity of the dispersed phase, microbeads did not form in any of these trials; thus subsequent trials dissolved cellulose in pure EMImAc. Based on prior work of ours ⁴² and Jo et al. ⁴⁴, cellulose was dissolved at 4% wt in all trials; higher solution concentrations had significantly higher viscosities and were difficult to process. ⁴² Finally, major processing parameters were fixed to further reduce the parameter space. As stirring at elevated temperatures (≥80 °C) led to discoloration of the cellulose solutions (Figure S12a), 40 °C was used for all future trials. Insufficient stirring – either due to low stir speed (below 250 RPM) or a small stir bar – led to dead volume in the reactor, resulting in a ring of solid cellulose forming instead of microbeads (Figure S12b). Thus a sufficiently large impeller and a stir speed of 250 RPM were selected for larger-scale trials; higher stir speeds could potentially be used to further reduce the microbead size.

After fixing the aforementioned parameters, the critical factors in the success of the emulsion system were the amount and rate of ethanol addition, and the initial ratio of cellulose/IL solution to oil. Based on small-scale trials, a ratio of 5:1 oil:cellulose solution was selected, as a 2.5:

1 ratio proved to be too little oil to adequately disperse IL. However, this 5:1 ratio may be able to be further reduced, as use of an impeller in larger-scale trials was significantly more effective for dispersing the cellulose solutions and no dead volume was observed in these trials. Following stirring, the heat was turned off and ethanol was added to precipitate the beads. Here, a 20:1 weight ratio of ethanol:cellulose solution was used to ensure complete bead precipitation; see SI.14 for trials using lower weight ratios. Ethanol was added at ~2-3 drops/s to slowly change the emulsion ethanol content and only minimally disrupt the flow. Stirring was then turned off, and beads were allowed to settle overnight into an intermediate layer between ethanol and oil. A scanning electron microscopy (SEM) image of a representative bead and the associated microbead diameter distribution for these standard conditions are shown in Figure 2.

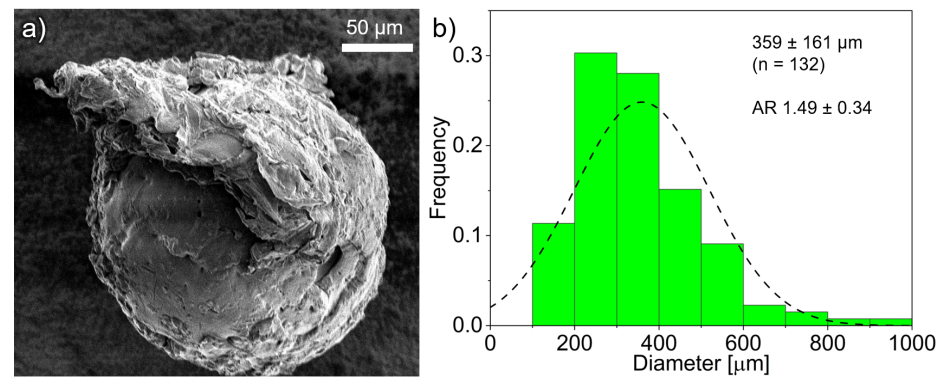


Figure 2: a) SEM images of cellulose microbeads produced from standard processing conditions (250 RPM, 2 h, 40 °C, 4% wt cellulose) reveal an approximately spherical shape with some larger inhomogeneities distributed irregularly across the surface. b) Bead diameters, D, are shown with a normal distribution (dashed line) superimposed. Bead diameters are broadly distributed, with a number-averaged D of 359 \pm 160 μ m and an average aspect ratio (top view) of 1.49 \pm 0.34.

Initially, microbeads were removed from the emulsion by gravity filtration, and were washed with ethanol and hexanes, followed by a Soxhlet extraction overnight using ethanol to remove residual IL. The removal of this IL reduced the average diameter of the microbeads by ~50% (SI.7), consistent with the size reduction seen via the dripping-precipitation process. ⁴² Complete IL removal was confirmed via energy-dispersive X-ray spectroscopy (EDS) (Figure S7). Unlike in prior works, ^{44,45} this system is surfactant-free and all IL is removed; thus the final product should be nearly pure cellulose, allowing for greater safety and environmental compatibility. Additionally, these beads have swelling ratios near unity and high gel fractions in water of ~0.9 (SI.13),

suggesting good potential stability in PCCPs.

The beads produced by this procedure were approximately spherical, with a small degree of surface roughness as well as some larger inhomogeneities likely resulting from deformation during the precipitation process. Porosity was not visible by electron microscopy. The beads were measured by image analysis, detecting the edges of the beads as viewed from above and fitting these shapes to ellipses. Based on the areas of these ellipses, the number-average bead diameter was 359 \pm 161 μ m, and based on the ratios of major to minor axis length, the average aspect ratio was 1.49 \pm 0.34. The majority of the beads produced in this manner had diameters within the target range to be competitive with commercial plastic microbeads ($D = 200-800 \, \mu$ m).

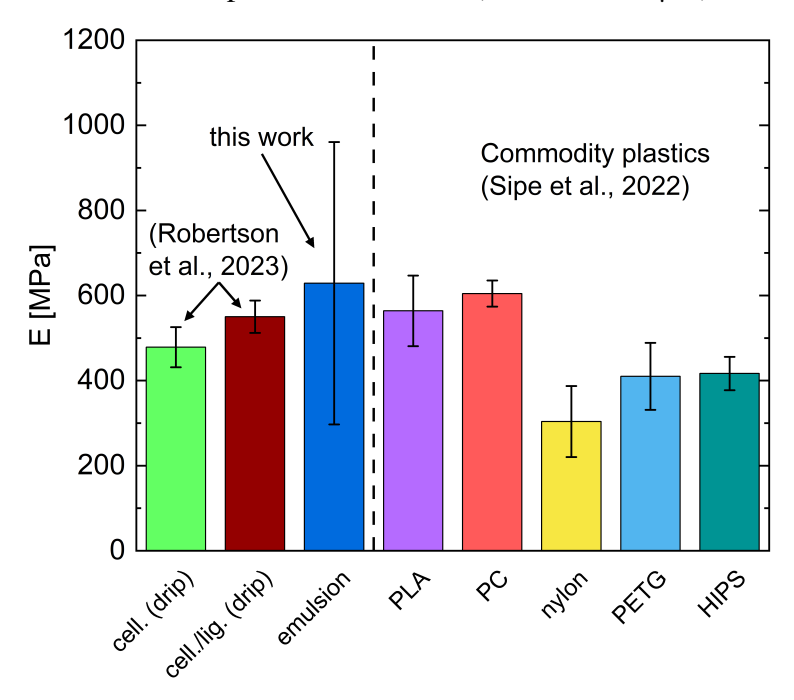


Figure 3: Comparison of the Young's modulus E for biomass beads produced via dripping method (Robertson et al. 42) and emulsion method (this work) with commodity plastics used in commercial microbeads analyzed by Sipe and coworkers. 8 Commodity plastics used are polylactic acid (PLA), polycarbonate (PC), nylon, polyethylene terephthalate glycol (PETG), and high-impact polystyrene (HIPS). The larger error bars for the emulsion method were due to the use of AFM on samples with rough surfaces (SI.8)

Furthermore, the average Young's modulus, E, of the beads produced by this emulsion process is similar to that of larger biomass beads ($D \sim 1$ mm) produced via a dripping method⁴² and to that of commodity plastics commonly used in commercial microbeads (Figure 3) – a promising indication of the value of these beads as exfoliants and rheological modifiers in consumer products.

Due to the small size of the microbeads produced by emulsion, single particle compression could not be used to measure Young's moduli as had been done for larger microbeads. 42 Instead, atomic force microscopy (AFM) was used to determine E. Due to the high surface roughness of these smaller beads, more variance was seen in these measurements than in single particle compression trials on larger microbeads (Figure 3), shown by larger error bars indicating the standard deviations in E.

Altering process parameters to mitigate bead aggregation

While the number-average diameter of the gravity-filtered process was within the appropriate range, sieving experiments revealed that much of the cellulose mass was contained within large, many-bead aggregates of >850 µm diameter (Table S3). These aggregates could not be broken up by sonication or other agitation methods. To determine if these aggregates were forming during the emulsion process or during purification, both processes were re-visited. As Jo et al. 44 used 5% Span 80 as a surfactant to stabilize cellulose emulsions, this surfactant was then added to the emulsion process. Sieving experiments following the emulsion and purification process reveal that 5% Span 80 addition does not impact the average microbead size for beads of average diameter below 850 µm (SI.11). However interestingly, Span 80 addition leads to a higher fraction of many-bead aggregates – suggesting that the formation of these large aggregates occurs during the purification process rather than in the emulsion. SEM images also reveal that 5% Span 80 addition leads to a slight change in the microbead surface topology (SI.11). Incorporating a different nonionic surfactant, polysorbate 20 (Tween 20), into the oil phase did not increase aggregation or have significant morphological effects (Figure S16), and in some cases minorly improved microbead yield (SI.6). However, incorporating this surfactant did not improve the surface morphology or reduce the average bead diameter. As surfactant use provided no substantial benefits in either case, no surfactant was used in future trials.

Additional emulsion trials purified via a faster filtration process suggested that the prolonged exposure to the atmosphere resulted in bead aggregation, likely due to interactions between residual

IL in the beads (Figure S7) and the water in the atmosphere. Some samples prepared in this way had mass fractions of as low as 10% of particles smaller than 850 μm (Table S3). To address this problem, several changes were made in the procedure (Figure 4): emulsions were poured into a separatory funnel to remove the bottom layer of oil and speed up the filtration process, and the ethanol and cellulose layers were filtered quickly by vacuum filtration, while washing with hexanes and acetone. Acetone is a stronger anti-solvent for cellulose, ⁴² so its use for washing helped de-swell beads more quickly, preventing clumping, and allowing yields of over 90% of particles smaller than 850 μm (SI.6). Note that both the changes to the filtration process and rinsing process were required to maximally increase yield (Table S3). However, no large morphological differences were seen between the two filtration and washing procedures (Figure 4b). Additionally, no significant differences in number-averaged microbead size were observed, as most of the mass in the original procedure was contained in a few large aggregates.

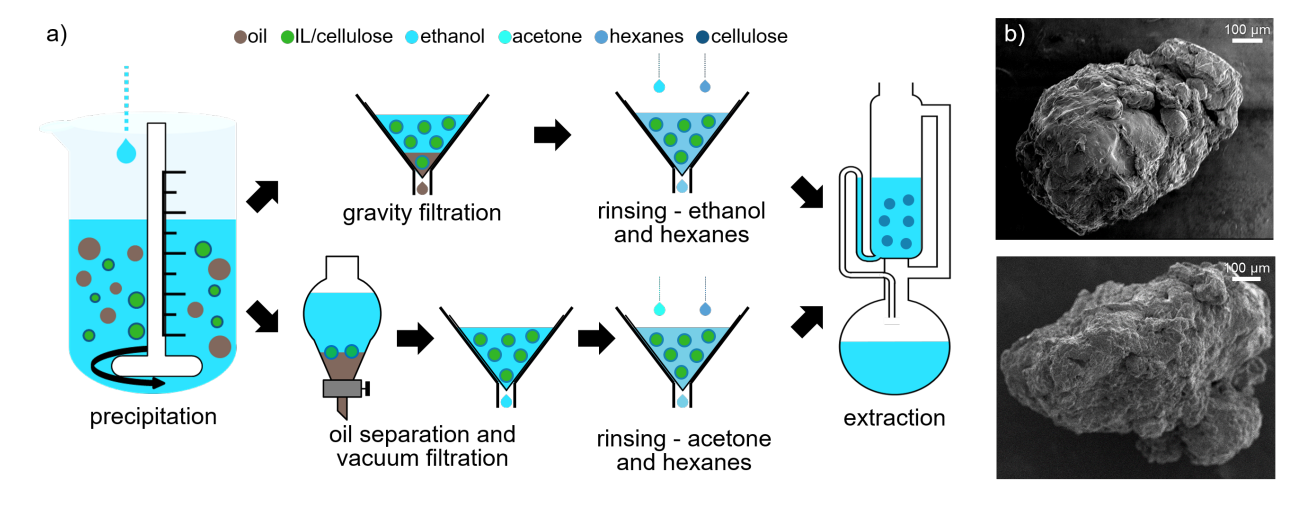


Figure 4: a) To promote faster bead filtration and reduce clumping during purification, an oil separation step was added and the ethanol wash was replaced with an acetone wash and vacuum filtration. b) No major differences in bead shape or surface morphology can be seen between the original process (top) and modified process (bottom).

Incorporating lignin into microbeads

To determine how robust this process was to biomass source, Kraft lignin was next incorporated into the cellulose solutions. While incorporating lignin at concentrations up to 50% wt of total

solution biomass ($f_{lignin} = 0.5$) does produce microbeads, the bead shape becomes progressively less spherical and the beads imaged via SEM appear more flaky with increasing f_{lignin} (Figure 5a). Lignin incorporation is also associated with more severe aggregation issues upon purification (SI.6). Aggregation can be clearly seen for $f_{lignin} = 0.33$ in Figure 5a, where two beads are stuck together except for a small crack, and for $f_{lignin} = 0.50$, where a number of smaller beads form a large aggregate. This trend can broadly be explained in terms of the higher solubility of Kraft lignin in oil, ⁵³ leading to lower emulsion stability and less well-defined drop interfaces which prevented interfacial tension measurement (SI.4). However, lignin incorporation did not impact the number-average bead diameter (Figure 5b).

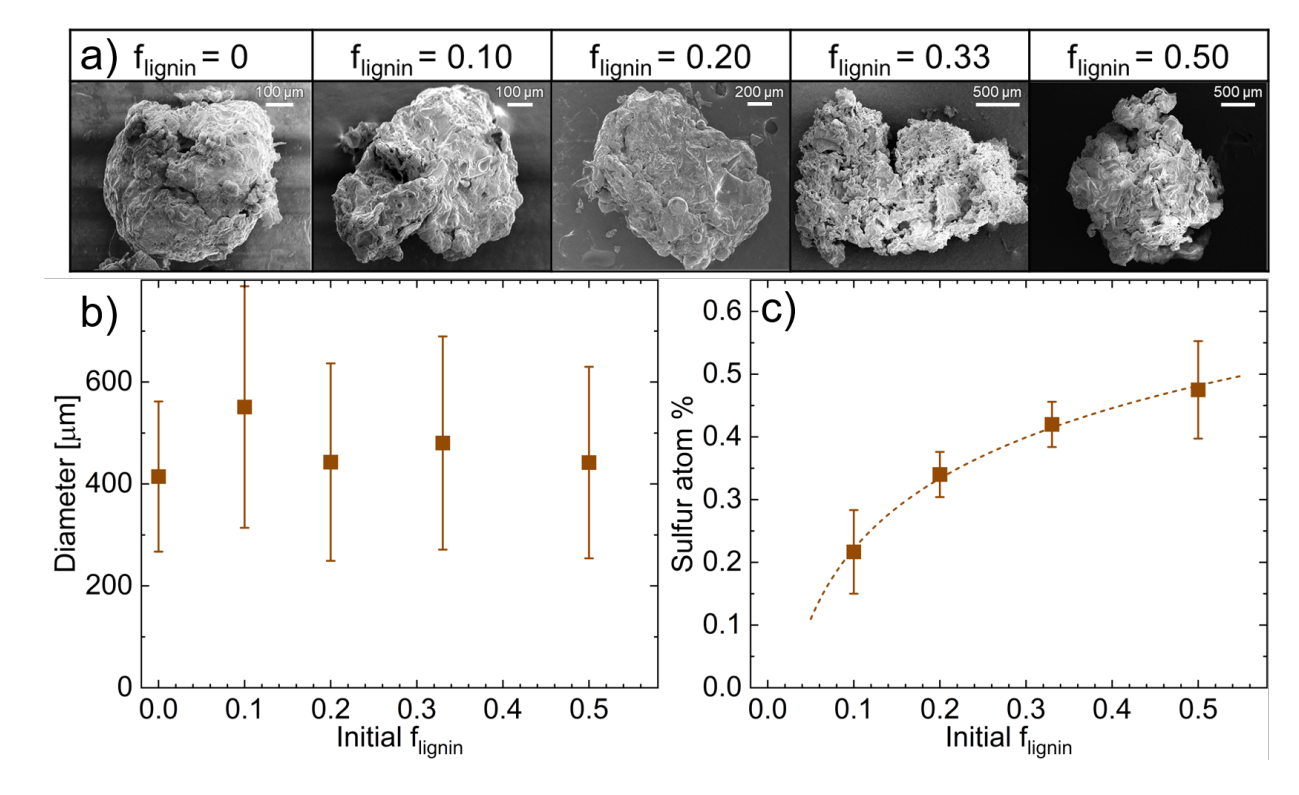


Figure 5: a) SEM images of microbeads with increasing lignin content show a destabilization of the emulsion with increased lignin concentration in the IL solution, f_{lignin} , resulting in less regular surface morphology and more aggregation. Images of higher lignin content beads are at lower magnification, showing an aggregate of several beads. b) Despite bead aggregation, the number-average bead diameter is independent of lignin content. c) EDS reveals that the sulfur atom % in the lignin beads increases with f_{lignin} according to atom % sulfur = 0.16 ln(f_{lignin}) – 0.15.

Energy dispersive X-ray spectroscopy reveals that although the lignin is soluble in oil phase, significant lignin content remains in the final microbead. Here, sulfur content indicates the pres-

ence of lignin, as Kraft lignin contains 2-3% sulfur (Figure S17). ⁵⁴ EDS measurements show that the sulfur composition of the beads increases with lignin concentration in the initial biomass solution (Figure 5c). However, this increase in microbead sulfur content is not linear with f_{lignin} in the biomass solution and instead begins plateauing at higher lignin contents, indicating that less of the lignin remains in the beads as more lignin is added to the solution. As such, this data is described well by a Freundlich isotherm (Figure 5c) consistent with dissolution of lignin into the bulk from a heterogeneous surface. ⁵⁵ To estimate the fraction of lignin retained in the beads, a lignin sulfur composition of 2.5% was assumed, based on EDS on the lignin powder (Figure S17). While all the lignin remains in the microbeads when the initial $f_{lignin} = 0.1$, around 70% of the initial lignin remains in the final bead from an initial $f_{lignin} = 0.2$, and only ~50% of the initial lignin remains in the final bead from $f_{lignin} = 0.33$ (Table S4). Perhaps unsurprisingly, this trend is remedied by the use of 5% Span 80 surfactant (Figure S15, Table S5), where measured beads retained all of the initial lignin. However as previously detailed, incorporating surfactant can cause difficulties with the work-up and extraction process (Figure S13), lowering the yield of microbeads within the target size range.

Qualitatively, the increase in lignin also caused the microbeads to become more brittle, in agreement with the trend observed in our prior work using the dripping synthesis. ⁴² Beads made from pure cellulose retained their structural integrity during imaging and did not collapse during transfer. However, as lignin concentration increased, beads or bead aggregates began to crumble between transfers. This behavior was most apparent when loading beads onto carbon tape for the SEM, as many beads containing large amounts of lignin crumbled while being adhered, beginning between f_{lignin} of 0.2 and 0.33. Quantitative differences between Young's moduli of lignin-containing and pure cellulose beads could not be determined, due to the flaky surface of beads with high lignin content. These features meant that tips used for atomic force microscopy (AFM) frequently broke when approaching the surface of the bead, preventing measurements on whole beads like those shown in Figure 3. However, upon fixing and sectioning these microbeads, average E values for these beads were also ~0.5 GPa, on par with the values observed for commod-

ity plastics and for larger biomass microbeads produced by compression; ^{8,42} see SI.8 for additional AFM data and details.

Modulating bead morphology via oil type

Emulsions incorporating a wide range of oils can successfully produce biomass microbeads; however, profound morphological differences can be seen as a result of oil choice. Microbeads have number-averaged diameters around 400 μ m, with particle aspect ratios from 1 to 2. For the standard conditions in this work (250 RPM stirring at 40 °C), using mineral oil results in semi-spherical beads as seen by SEM (Figure 6, first row). These microbeads have a number-averaged diameter of 359 \pm 161 μ m, with an average aspect ratio of 1.49 \pm 0.34 and an average surface roughness, $R_{q,norm}$, of 1.04 \pm 0.04 (Table 1). A closer look at their surface topology reveals no regular pore structure or well-defined pattern (Figure 6, second row), resulting in the low measured roughness.

Switching to a ten-fold higher viscosity oil, S600, as the oil phase results in less spherical beads (Figure 6, second column). Notably, while the oil viscosity changes substantially, the interfacial tension between this oil and the IL solvent, $\sigma_{oil,IL}$, is approximately equal to that between the mineral oil and IL solvent (Table 1). The resulting microbeads have a number-averaged diameter of 276 \pm 191 μ m, with an average aspect ratio of 1.94 \pm 0.70. More closely examining the bead surface reveals small bumps or wrinkles which make the bead look rougher at higher magnification (Figure 6, second row). As a result of these features, the average surface roughness, $R_{q,norm}$, of these beads is 1.13 \pm 0.12. This roughness value is significantly higher (p < 0.05) than that for beads produced in mineral oil, based on a one-tailed t-test.

Mixing mineral oil and S600 (3:1 mineral oil to S600 by volume) results in an interfacial tension, $\sigma_{oil,IL}$, similar to its two components, but a viscosity much closer to that of mineral oil. Use of this mixture as the oil phase in the emulsion results in microbeads with visible protrusions (Figure 6, third column). These surface protrusions are larger and more spherical than those formed on the S600 beads, but these features are still fused to the bulk of the bead. These beads have a number-averaged diameter of $382 \pm 224 \, \mu m$, with an average aspect ratio of 1.63 ± 0.48 and

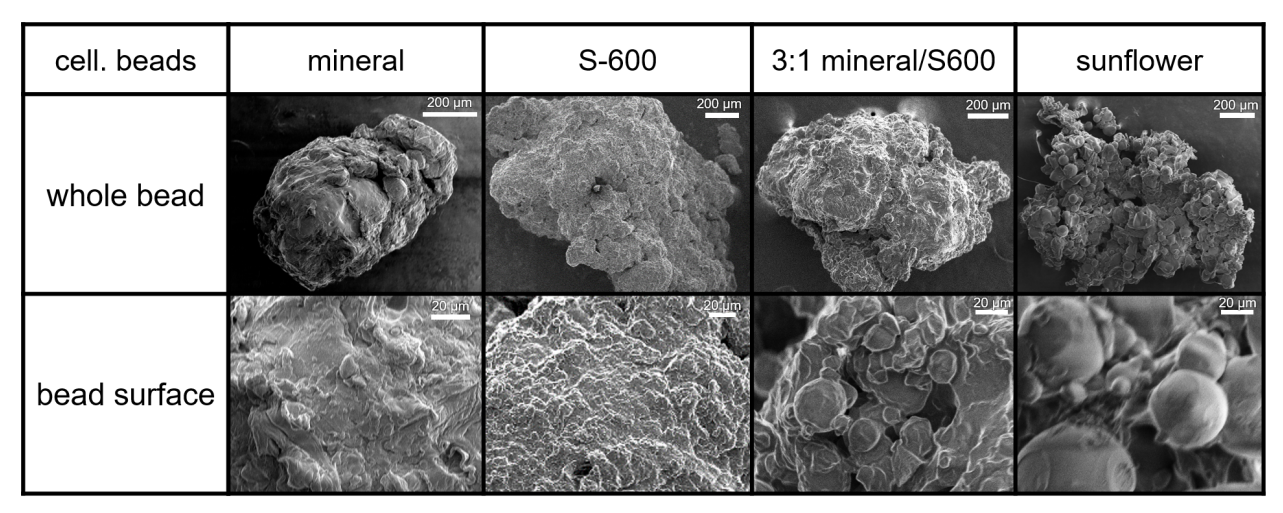


Figure 6: Images of microbeads (first row) and microbead surfaces (bottom row) from emulsions of 4% wt cellulose in EMImAc and various oils. Scale bars are $200 \, \mu m$ in the top row and $20 \, \mu m$ in the bottom row. Microbeads made in mineral oil have the smoothest surfaces; rougher surfaces are seen for the other oils, with more pronounced protrusions appearing from left to right.

an average $R_{q,norm}$ of 1.11 \pm 0.03. Although the $R_{q,norm}$ is similar in value to that for the S600 beads, this overall variance results from large changes in the surface around the boundaries of the protrusions, rather than small changes distributed more evenly as on the surface of the S600 beads. On the protrusions, or in between the protrusions, the surface of the 1:3 mineral:S600 beads appears smoother than the surface of the S600 beads.

Use of sunflower oil results in the most interesting morphology; this oil has a lower viscosity and $\sigma_{oil,IL}$ than the previous three oils (Table 1). Here, the microbeads have small, spherical growths attached to the bead surface. These growths range in diameter from around 10 μ m to 100 μ m. The main microbeads have a number-averaged diameter of 449 \pm 244 μ m, with an average aspect ratio of 1.63 \pm 0.43 and an average $R_{q,norm}$ of 1.08 \pm 0.09. Though not significantly smoother than the microbeads produced in 3:1 mineral oil to S600, the decrease in average roughness here can be attributed to the increase in the size of the spherical growths, as the surface of these protrusions is relatively smooth. The morphology of these beads resembles real plastic microbeads recovered from commercial products, ¹⁹ and may be helpful for gentle exfoliation without causing abrasions to skin.

Moving from left to right in Figure 6, the surface of the beads becomes less smooth and the spherical growths become larger and more pronounced; for example, the surfaces of the beads

Table 1: Properties of oils used in emulsions, including viscosity (η_{oil}) , interfacial tension with 4% wt. cellulose/IL solution $(\sigma_{oil,cell/IL})$, with IL $(\sigma_{oil,IL})$, and with ethanol $(\sigma_{oil,eth})$, and change in interfacial tension due to the addition of cellulose to IL $(\Delta\sigma_{cell})$. The properties of the resulting microbeads are also given: diameter, aspect ratio, and surface roughnesses $(R_{q,norm})$. Uncertainties are expressed as the standard deviation across trials, except for the error in $\Delta\sigma_{cell}$, which was determined from the errors in $\sigma_{oil,cell/IL}$ and $\sigma_{oil,IL}$.

oil	mineral	S600	3:1 mineral:S600	sunflower
$\eta_{25,oil}$ [mPa·s]	150	1100	229	67
$\sigma_{oil,cell/IL}$ [mN/m]	14.36 ± 1.32	5.78 ± 0.21	6.57 ± 0.24	2.26 ± 0.02
$\sigma_{oil,IL}$ [mN/m]	5.65 ± 1.00	5.86 ± 0.12	5.46 ± 0.10	2.63 ± 0.06
$\Delta\sigma_{cell}$ [mN/m]	8.71 ± 1.65	-0.08 ± 0.24	1.12 ± 0.26	-0.37 ± 0.06
$\sigma_{oil,eth}$ [mN/m]	2.31 ± 0.12	5.15 ± 0.12	5.16 ± 0.14	1.38 ± 0.09
diameter [µm]	359 ± 161	276 ± 191	382 ± 224	449 ± 244
aspect ratio	1.49 ± 0.34	1.94 ± 0.70	1.63 ± 0.48	1.63 ± 0.43
roughness $(R_{q,norm})$	1.04 ± 0.04	1.13 ± 0.12	1.11 ± 0.03	1.08 ± 0.09

produced in mineral oil are the smoothest, whereas the other three oils produce beads with similar $R_{q,norm}$ but the protrusion size increases for beads made from S600 (smallest) through sunflower oil (largest). Table 1 is arranged in the same order as Figure 6, suggesting that the surface morphology is not a function of the oil viscosity only, as the viscosities do not trend in this same manner. On the other hand, the surface morphology does seem strongly related to the interfacial tension between the cellulose solution and the oil ($\sigma_{oil,cell/IL}$), with lower $\sigma_{oil,cell/IL}$ corresponding to a more wrinkled surface or more pronounced spherical growths.

One possible explanation for the trend between bead morphology and interfacial tension is that oils with lower $\sigma_{oil,cell/IL}$, like sunflower oil, may have stronger interactions with the cellulose dissolved in the IL – which could result in more cellulose being adsorbed to the droplet interface prior to microbead precipitation. Given that sunflower oil is a triglyceride vegetable oil, a stronger interaction with the highly polar IL and cellulose – versus the hydrocarbons that make up mineral oil – would be reasonable. The trend in surface morphology with interfacial tension is further supported when the difference in interfacial tension between oil and IL upon cellulose addition $(\Delta \sigma_{cell} = \sigma_{oil,cell/IL} - \sigma_{oil,IL})$ is examined. The interfacial tension between the IL and mineral oil increases significantly upon the addition of cellulose (from $\sigma_{oil,IL}$ to $\sigma_{oil,cell/IL}$; Table 1), whereas the interfacial tension between IL and sunflower oil decreases upon cellulose addition. This increase

in interfacial tension, which is well-documented in some cases of increasing salinity in water, ^{56,57} has also been seen previously in cellulose suspensions where the cellulose remains in the bulk. ⁵⁸ In contrast, surface-active cellulose is known to reduce interfacial tension. ⁵⁹ This evidence suggests that for emulsions in mineral oil, the dissolved cellulose is not highly surface active, whereas cellulose is most surface active in the emulsions containing sunflower oil; the other two oils exhibit intermediate behavior but are more similar to the behavior observed in the sunflower oil emulsions.

Factors controlling interfacial properties during precipitation

To confirm the hypothesis that more cellulose is at the droplet interface in some oils than in others, drops of cellulose/IL solution were extruded into each of the four oils shown in Table 1. Here, the thinning and breakup of the droplet neck was imaged, and the minimum radius (R_{min}) of the neck was extracted using image analysis, in an analogous method to capillary-driven thinning experiments. This experiment mimics (on a larger scale) the basic deformation involved in breaking up drops in the emulsion. Due to the presence of cellulose in the system, this deformation may be resisted by elastic forces, which are present when polymer coils are deformed. If these forces are strong enough, the thinning would occur in an apparent "elasto-capillary" (EC) regime. Here, R_{min} decreases exponentially in time according to the following equation, where R_0 is the radius of the needle, K is a fitting constant, and λ_E is the apparent extensional relaxation time:

$$\frac{R_{min}}{R_0} = Kexp\left(\frac{-t}{3\lambda_E}\right) \tag{3}$$

This relaxation time λ_E is a characteristic time which corresponds to the elasticity of the fluid: the more elastic the fluid is, the higher the value of λ_E . However, this elastic behavior resulting in an apparent EC regime could originate from bulk elasticity or interfacial elasticity. Thus to confirm that differences in dripping behavior reflect differences in the interface resulting from the presence of cellulose, significant bulk elasticity must be ruled out.

Images from dripping IL droplets into sunflower oil both without and with dissolved cellulose

(Figure 7a and b, respectively) reveal that the presence of cellulose strongly impacts the thinning behavior of the droplet neck. The pure IL droplet breaks up with minimal elongation (Figure 7a), pinching off at both ends of the neck. This behavior is characteristic of low-viscosity Newtonian fluids in an outer oil. Conversely, the cellulose solution droplet elongates significantly after leaving the nozzle (Figure 7b); here, thinning occurs in a long, slender neck – a shape characteristic of elastic fluids undergoing elastocapillary-like thinning (Equation 3). The expected exponential decay of R_{min} for elastic fluids is also present when cellulose/IL is dripped into the other three oils (Figure S5). This behavior is in contrast to capillary-driven thinning experiments performed in air for our previous work with an 8% wt. solution of the same cellulose. In those experiments, no elasticity was observed during liquid bridge thinning and breakup, despite the sample having twice the cellulose content as the solution used here – suggesting that the elasticity observed in the dripping experiments in Figure 7 is due to interfacial, not bulk, elasticity.

Beyond the changes in interfacial interactions that result when changing the oil type in these dripping experiments, the viscosity of the oil through which the cellulose/IL drop moves changes. For Newtonian outer fluids like these oils (Figure S9), the viscosity of the outer fluid should not affect a pure capillary thinning process. $^{61-63}$ However, the bottom of the droplet is falling through fluids of different viscosity, which occurs more slowly for higher viscosity fluids. 64 Thus to accurately compare the different values of the apparent λ_E resulting in different oils, λ_E was normalized by the viscosity ratio between the oil and the cellulose solution, $\frac{\eta_{oil}}{\eta_{cell/IL}}$, as has been done for dimensionless parameters describing extensional flow. 63 These reduced extensional relaxation times ($\lambda_{E,reduced} = \lambda_E \frac{\eta_{cell/IL}}{\eta_{oil}}$) are plotted in order of the resulting bead morphology in Figure 7b, from left to right based on increasing deviations from a smooth spherical bead (increasing surface roughness, then larger spherical growths). These $\lambda_{E,reduced}$ values also increase from left to right (Figure 7b) – following a trend opposite to that for the interfacial tension between the cellulose/IL solution and oil ($\sigma_{oil,cell/IL}$). These apparent relaxation times indicate a higher elasticity of the interface between oil and cellulose/IL droplet – and thereby more cellulose adsorbed to the interface – in the emulsions that form beads with more pronounced surface inhomogeneities. These results are

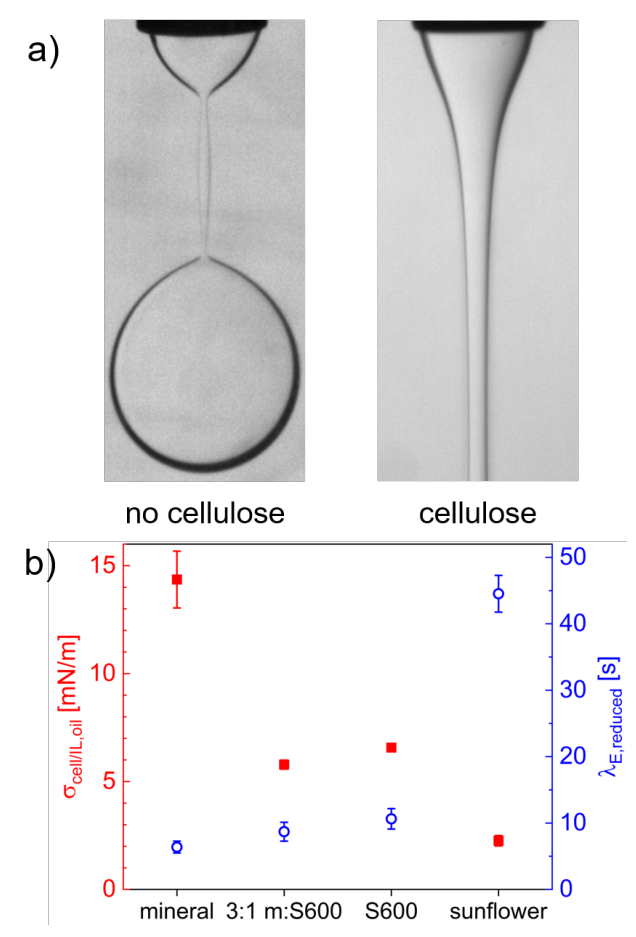


Figure 7: a) Images during dripping of (L) pure IL in sunflower oil and (R) cellulose/IL solution in sunflower oil show a rapid pinch-off of pure IL but an elongated neck generally associated with elasticity in capillary thinning ⁶⁰ when cellulose is present, unlike in capillary thinning of cellulose solutions in air. ⁴² b) Beads with more pronounced surface features are made from oils with lower interfacial tension ($\sigma_{oil,cell/IL}$) and higher elasticity ($\lambda_{E,reduced} = \lambda_E \frac{\eta_{cell/IL}}{\eta_{oil}}$) indicating a thicker layer of cellulose adsorbed at the interfaces of these oils.

also consistent with the hypothesis developed based on interfacial tension measurements – that the dissolved cellulose is not highly surface active in mineral oil emulsions and is most surface active in sunflower oil emulsions.

Proposed mechanisms dictating surface morphology

To relate this phenomenon of higher interfacial elasticity to the formation of the observed microbead surface morphologies, the mechanism of microbead precipitation is considered. As ethanol is immiscible with all oils used (SI.2), the precipitation of the cellulose/IL solution drops must occur through a transient double emulsion, i.e. an emulsion containing dispersed droplets of both ethanol and cellulose/IL in oil. The precipitation process involves an ethanol drop coming into contact with a cellulose/IL drop for some period of time so that IL and ethanol can counter-diffuse. 65,66 Although this process does not occur at equilibrium, an equilibrium double emulsion framework is useful for approximating what this contact might look like.

Depending on the interfacial tensions between each pair of phases in the system, double emulsions can be described as either non-engulfing, partially-engulfing, or fully engulfing (Figure 8a). In non-engulfing double emulsions, the two dispersed phases do not contact each other at equilibrium. For partially engulfing emulsions, a limited contact area occurs between the two dispersed phases; for fully engulfing emulsions, the dispersed phase with a lower σ (with the continuous phase) covers the drop of the other dispersed phase. The morphology that the double emulsion assumes is determined by spreading coefficients of the oil, cellulose/IL, and ethanol phase S_{oil} , $S_{cell/IL}$, and $S_{ethanol}$, defined based on the surface tensions between oil and cellulose/IL ($\sigma_{oil,cell/IL}$), oil and ethanol ($\sigma_{oil,eth}$), and cellulose/IL and ethanol ($\sigma_{cell/IL,eth}$) as follows: 67,68

$$S_{oil} = \sigma_{cell/II,eth} - \sigma_{oil\,cell/II} - \sigma_{oil\,eth} \tag{4}$$

$$S_{cell/IL} = \sigma_{oil,eth} - \sigma_{oil,cell/IL} - \sigma_{cell/IL,eth}$$
(5)

$$S_{ethanol} = \sigma_{oil,cell/IL} - \sigma_{oil,eth} - \sigma_{cell/IL,eth}$$
 (6)

According to a theory proposed by Johnson and Sadhal, ⁶⁸ a double emulsion will be fully engulfing when $S_{oil}/\sigma_{oil,ethanol} \leq -2$. Based on the spreading coefficients for this system (Table S2), the ethanol drops should fully engulf the cellulose/IL drops at equilibrium for all oils. Here, the normalized value for the S600 ($S_{oil}/\sigma_{oil,ethanol} = -2.12$) is the closest to the critical value of -2. These predictions also agree with the results from Torza and Mason, based on the values of all three spreading coefficients (Table S2). ⁶⁷ Although this result is for emulsions at equilibrium, the fully engulfing morphology means that ethanol is likely fully surrounding the cellulose/IL drop during precipitation in this system as well.

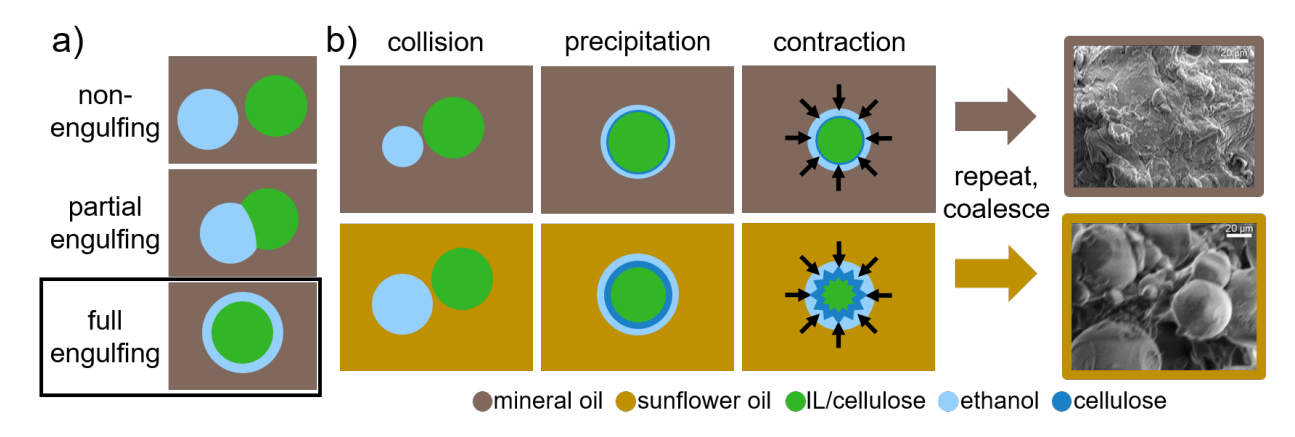


Figure 8: a) Equilibrium emulsion morphology depending on spreading coefficients, based on criteria from Torza and Mason⁶⁷ and Johnson and Sadhal.⁶⁸ Light blue drops represent ethanol, green drops represent IL/cellulose solution, and the brown background represents the continuous oil phase. b) In sunflower oil, the larger quantity of cellulose adsorbed at the interface of the IL droplet causes a thicker layer of semi-solid cellulose to precipitate upon initial contact with the ethanol phase. During precipitation, as the drops shrink and lose solvent, the thicker interface in sunflower oil buckles more, leading to surface inhomogeneities which coalesce into spheres.

Because the double emulsion in this system is fully engulfing at equilibrium, the ethanol drop should quickly spread and cover the cellulose/IL drop after collision (Figure 8b). As the layer of ethanol spreads across the cellulose/IL surface, an outer layer of cellulose should precipitate. As shown in Figure 8b, this layer of precipitated cellulose will be thicker for cellulose/IL droplets in oils with higher interfacial elasticity and lower interfacial tension, like sunflower oil, than for those in mineral oil. After this initial layer forms, the ethanol diffuses in and the IL diffuses out of the droplet, 65,66 causing the precipitating drop to shrink. As the drop shrinks, the semi-solid layer of cellulose on the surface will buckle, likely causing the observed inhomogeneities on the surface

(Figure 8b). This process occurs in all the oils; however, given the higher $\sigma_{oil,cell/IL}$ and lower $\lambda_{E,reduced}$ values in mineral oil, the cellulose should be less surface active, such that the droplet can shrink relatively uniformly with minimal buckling, resulting in a comparatively smooth surface of the final bead. On the other hand, the higher surface activity of cellulose in sunflower oil means that there is more cellulose and less IL at the surface relative to the bulk. This interfacial layer of cellulose buckles more than for mineral oil and is slower to coalesce into a fully spherical bead. Therefore, the interfacial properties in sunflower oil likely cause the spherical growths on the surface of the primary bead, rather than leading to a single spherical bead. Similar inhomogeneities are seen for beads formed from S600 and 3:1 mineral:S600.

The mechanism described above assumes that the ethanol drop spreads quickly and immediately engulfs the cellulose/IL drop; this assumption is the weakest in S600 emulsions for two reasons. First, $S_{oil}/\sigma_{oil,ethanol}$ is the closest to the critical value of -2 and thus closest to an equilibrium partial engulfing morphology (Table S2). Second, to spread across the surface of the cellulose/IL drop, the ethanol droplet needs to diffuse through and displace S600 – which does not occur instantaneously given that S600 is more viscous by three orders of magnitude. Considering how the emulsion may deviate from the equilibrium morphology in S600 may help explain some differences between beads formed in S600 vs. 3:1 mineral:S600. Although $\sigma_{oil,cell/IL}$ and $\Delta\sigma_{cell}$ are slightly lower for S600 than for 3:1 mineral:S600 and the $\lambda_{E,reduced}$ values are within uncertainty of one another, the S600 beads do not exhibit the clear spherical growths that are observed on beads produced in 3:1 mineral: \$600. If ethanol spreading and diffusion occurs sufficiently slowly in an S600 emulsion due to the high S600 viscosity, precipitation that occurs in one location on the cellulose/IL droplet could locally wrinkle the surface while forcing cellulose/IL solution to the opposite side of the droplet. This effect could mitigate some of the cellulose layer buckling that occurs in 3:1 mineral:S600 and sunflower oil, which leads to the large spherical growths observed on those beads. This process would also result in more elongated beads, with higher average aspect ratios, which is the trend observed for \$600 beads (Table 1).

While the above mechanism does adequately explain the morphologies produced by different

oils, multiple other possible explanations could explain this phenomenon. For example, given the transient double emulsion formed during precipitation, the collision of small ethanol drops with larger cellulose solution droplets could result in the precipitation of small areas of the cellulose solution surface. On the other hand, coalescence of smaller beads that initially precipitate could lead to a similar structure. As both of these alternate mechanisms rely on the sizes of the ethanol and cellulose solution drops in the double emulsion, a framework to predict these sizes is necessary.

The size of the droplets in this kind of emulsion is determined by an equilibrium between droplet breakup and coalescence of droplets of a dispersed phase in contact with an immiscible continuous phase. Droplets break up when the applied deformation resulting from the mixing is large enough to overcome the viscosity and surface tension that resist this deformation. ^{52,69} Here, the droplet size is approximated by the largest droplet size that will not break up under this deformation. Deformations involved in mixing are generally turbulent, involving both shear and extensional flows; however, droplets will not break up in simple shear when the ratio of dispersed phase viscosity to continuous phase viscosity ($r = \eta_D/\eta_C$) is greater than 4. ⁶⁹ Given that viscosity ratios of the cellulose solution exceed 4 for all oils used (Figure S9) and the fact that emulsions form in all cases, an extensional mode of drop breakup is likely dominant, consistent with literature studies of drop size distributions in emulsions. ⁵²

Extension-induced breakup in this system is determined by a critical value of the capillary number (Ca_E) above which breakup will occur. Ca_E is determined by the following expression, in which $\dot{\epsilon}$ is the extension rate, D_E is the maximum diameter of the dispersed droplets, η_e is the viscosity of the emulsion, and σ is the interfacial tension between the two phases:⁵²

$$Ca_E = \frac{\dot{\epsilon}D_E \eta_e}{2\sigma} \tag{7}$$

Equation 7 only applies to the system before microbeads have precipitated, so the relevant viscosity for this calculation is the emulsion viscosity early in the precipitation process (see Figure 1). This viscosity should be nearly the same for both the cellulose/IL and ethanol droplet phases due to oil comprising the majority of the emulsion volume before most of the ethanol is added. The ex-

tension rate is also equivalent for both the cellulose/IL and ethanol phases, as the phases coexist in the same flow. The other relevant factors in determining the droplet size that would differ between the cellulose/IL and ethanol phases would be the critical capillary number (Ca_E) and the interfacial tension σ . In extensional flow, the critical capillary number for breakup reaches a limiting value of 0.11 for high viscosity ratios, and is generally not larger than 0.25 even for very low ($p \sim 10^{-3}$) viscosity ratios. Therefore, differences in critical capillary number for cellulose/IL and ethanol phases should not affect the ratio of drop diameters of the two dispersed phases by more than a factor of approximately 2. Consequently, the ratio $R = \frac{\sigma_{oil,IL}}{\sigma oil,eth}$ of interfacial tensions between each dispersed phase and the continuous oil phase should approximately be proportional to the ratio between the diameters of the oil and ethanol droplets.

Based on the measured interfacial tensions between phases, the dispersed drops of ethanol and cellulose solution should have similar sizes for all of the oils except mineral oil (Table 1). Due to the high interfacial tension between mineral oil and cellulose solution, the drops of cellulose solution should be around six times the size of the ethanol droplets in a mineral oil emulsion. If the spherical growths on the bead surface were the result of smaller ethanol droplets colliding with the cellulose solution droplets, this droplet size prediction would not explain the surface morphologies seen in Figure 6; in fact, the beads formed in mineral oil might be expected to have more spherical growths due to this mismatch in droplet size. Not only are no spherical growths seen on mineral oil beads, but these beads are actually the smoothest. Additionally, emulsions in the other three oils are expected to have similar drop sizes – but the observed spherical growths are markedly different in size for each of these three cases – meaning that the differences in size between the ethanol and cellulose/IL drops cannot explain the observed morphologies.

Another possible mechanism to explain the presence of the spherical growths on the microbead surfaces is aggregation and coalescence. For example, the microbeads that initially form and precipitate in sunflower oil could be on the length scale of the small spherical growths. These beads could then aggregate and coalesce into larger beads later in the precipitation process or during purification, and this coalescence of smaller beads could result in the morphology observed in Figure

6. While coalescence and aggregation during precipitation and purification may be a contributing factor toward the observed morphology, coalescence is unlikely to explain the surface morphology of all microbeads. For example, the microbeads produced in S600 are rough and wrinkled, but these beads do not display any sphere-like growths or protrusions. Furthermore, a coalescence and partial fusion mechanism alone would likely not result in a single central microbead with small spherical growths as is observed in Figure 6 – but rather in many instances of several similarly sized beads fused together with no clear primary bead. As such, this aggregation and coalescence mechanism is likely not the primary driver of the observed microbead surface topology.

Conclusion

In this work, biomass microbeads with tunable surface morphologies and robust mechanical properties were prepared for the first time via a scalable, surfactant-free emulsion and precipitation process. Novel bead shapes and surface morphologies are achieved by altering the composition of the biomass solution and the interfacial properties of the emulsion oil phase. The resulting microbeads have Young's moduli on par with commodity plastics (~1 GPa), and are within the target size range to be effective in consumer products but be captured during wastewater treatment (200-800 µm diameter). During microbead production, some conditions resulted in >90% of biomass being incorporated into beads under 850 µm in diameter, although higher lignin content feedstocks decreased this yield. Lignin was successfully retained in microbeads at weight fractions up to 20% without significant leaching or emulsion destabilization; improved lignin retention at higher lignin weight fractions was observed with surfactant addition. Use of different oils resulted in a wide range of bead shapes and surface morphologies due to changing interfacial properties of cellulose. Dripping measurements and pendant drop tensiometry indicated that cellulose favors the bulk over the mineral oil/IL interface, which results in smooth beads as the cellulose/IL drops contract and precipitate. Conversely, the higher affinity of cellulose for the sunflower oil/IL interface results in formation of spherical growths on the microbead surface. This surface topology is likely due to buckling of the interfacial cellulose layer during precipitation, and the ability to produce this

morphology controllably may be useful for effective and gentle exfoliants.

While this method is currently not yet competitive in cost with commercial microbeads, the flexibility of the technique with respect to biomass feedstock composition and oil type, and the ability to tune the interfacial morphology, is promising for implementation at scale for certain target products. Cost-competitive scale-up of these microbeads will depend on the ease of IL recycling and the ability to reduce the cost of the inputs. The incorporation of lignin is promising for cost reduction, but a more ambitious long-term goal is the use of whole biomass – which would be more readily available and involve less pre-processing. Scaling up microbead production would also enable a wider range of studies, such as biodegradation or rheological and exfoliation tests to verify the microbead efficacy in model products; these tests require grams to kilograms of sample. Another test that would be enabled by scaling up bead production is measuring adsorption of target pollutants such as heavy metals. Thus beyond replacing petroleum-derived plastic microbeads, biomass microbeads in wastewater could provide a promising vector for passive contaminant remediation, given that most beads are recaptured during the wastewater treatment process.

Acknowledgement

The authors acknowledge the support of the National Science Foundation Center for Sustainable Polymers under Grant No. CHE-1901635, and the University of Minnesota Office of Technology Commercialization Early Innovation Grant. The authors thank the Michael H. Baker Foundation for their support of this project. The authors thank Dr. Michael Manno for training and use of the Valspar Materials Science and Engineering Laboratory for SEM and sizing measurements, and the Anton Paar VIP Program for use of their shear rheometers.

Supporting Information Available

The Supporting Information contains additional data and analyses, including: oil/ethanol miscibility studies; interfacial tension measurements and emulsion morphology calculations; radial decay

data from dripping measurements; additional data detailing filtration, washing, and extraction effects; atomic force microscopy measurements; Fourier transform infrared spectroscopy on beads and starting material; steady shear rheology and viscosity data; data on emulsion failure trials; additional studies on surfactant use; energy-dispersive X-ray spectra following lignin incorporation; *p*-values from statistical analyses; tables of variables and abbreviations.

References

- (1) Leslie, H. A. Review of microplastics in cosmetics. *IVM Institute for Environmental Studies* **2014**, *476*, 1–33.
- (2) Gambino, I.; Bagordo, F.; Grassi, T.; Panico, A.; De Donno, A. Occurrence of Microplastics in Tap and Bottled Water: Current Knowledge. *Int. J. Environ. Res. Public Health* **2022**, *19*, 5283.
- (3) Sridharan, S.; Kumar, M.; Singh, L.; Bolan, N. S.; Saha, M. Microplastics as an emerging source of particulate air pollution: A critical review. *J. Hazard. Mater.* **2021**, *418*, 126245.
- (4) Leslie, H. A.; van Velzen, M. J. M.; Brandsma, S. H.; Vethaak, A. D.; Garcia-Vallejo, J. J.; Lamoree, M. H. Discovery and quantification of plastic particle pollution in human blood. *Environ. Int.* 2022, 163, 107199.
- (5) Rochman, C. M.; Kross, S. M.; Armstrong, J. B.; Bogan, M. T.; Darling, E. S.; Green, S. J.; Smyth, A. R.; Veríssimo, D. Scientific Evidence Supports a Ban on Microbeads. *Environ. Sci. Technol.* 2015, 49, 10759–10761.
- (6) Cheung, P. K.; Fok, L. Characterisation of plastic microbeads in facial scrubs and their estimated emissions in Mainland China. *Water Res.* **2017**, *122*, 53–61.
- (7) Xanthos, D.; Walker, T. R. International policies to reduce plastic marine pollution from

- single-use plastics (plastic bags and microbeads): A review. *Mar. Pollut. Bull.* **2017**, *118*, 17–26.
- (8) Sipe, J. M.; Bossa, N.; Berger, W.; von Windheim, N.; Gall, K.; Wiesner, M. R. From bottle to microplastics: Can we estimate how our plastic products are breaking down? *Sci. Total Environ.* **2022**, *814*, 152460.
- (9) Coombs OBrien, J.; Torrente-Murciano, L.; Mattia, D.; Scott, J. L. Continuous Production of Cellulose Microbeads via Membrane Emulsification. ACS Sustain. Chem. Eng. 2017, 5, 5931–5939.
- (10) Habib, R. Z.; Salim Abdoon, M. M.; Al Meqbaali, R. M.; Ghebremedhin, F.; Elkashlan, M.; Kittaneh, W. F.; Cherupurakal, N.; Mourad, A.-H. I.; Thiemann, T.; Al Kindi, R. Analysis of microbeads in cosmetic products in the United Arab Emirates. *Environ. Pollut.* 2020, 258, 113831.
- (11) Napper, I. E.; Bakir, A.; Rowland, S. J.; Thompson, R. C. Characterisation, quantity and sorptive properties of microplastics extracted from cosmetics. *Mar. Pollut. Bull.* **2015**, *99*, 178–185.
- (12) Ziajahromi, S.; Neale, P. A.; Rintoul, L.; Leusch, F. D. L. Wastewater treatment plants as a pathway for microplastics: Development of a new approach to sample wastewater-based microplastics. *Water Res.* **2017**, *112*, 93–99.
- (13) Möhlenkamp, P.; Purser, A.; Thomsen, L. Plastic microbeads from cosmetic products: an experimental study of their hydrodynamic behaviour, vertical transport and resuspension in phytoplankton and sediment aggregates. *Elem. Sci. Anth.* **2018**, *6*, 61.
- (14) Kalčíková, G.; Alič, B.; Skalar, T.; Bundschuh, M.; Gotvajn, A. Z. Wastewater treatment plant effluents as source of cosmetic polyethylene microbeads to freshwater. *Chemosphere* **2017**, *188*, 25–31.

- (15) Shareef, M. Y.; Shareef, F. M. Y. Determination of Microbeads from Paste in Some Pharmaceuticals and Personal Care Products. *J. Pharm. Sci. Technol.* **2021**, *5*, 53.
- (16) Duis, K.; Coors, A. Microplastics in the aquatic and terrestrial environment: sources (with a specific focus on personal care products), fate and effects. *Environ. Sci. Eur.* **2016**, 28, 2.
- (17) Gan, H.; Okada, T.; Kimura, S.; Kasuya, K.-i.; Iwata, T. Manufacture, physical properties, and degradation of biodegradable polyester microbeads. *Polym. Degrad. Stab.* **2023**, 208, 110239.
- (18) Kitsongsermthon, J.; Duangweang, K.; Kreepoke, J.; Tansirikongkol, A. In vivo cleansing efficacy of biodegradable exfoliating beads assessed by skin bioengineering techniques. *Skin Res. Technol.* **2017**, *23*, 525–530.
- (19) Akhbarizadeh, R.; Yu, J. T.; Ead, L.; Nicholls, E.; Thibeau, J.; Lanisa, M.; Wakai, M.; Marquez, A.; Miller, C.; Sims, A.; Diamond, M. L.; Helm, P. A. Reductions of Plastic Microbeads from Personal Care Products in Wastewater Effluents and Lake Waters Following Regulatory Actions. *ACS ES&T Water* **2024**,
- (20) Praveena, S. M.; Shaifuddin, S. N. M.; Akizuki, S. Exploration of microplastics from personal care and cosmetic products and its estimated emissions to marine environment: An evidence from Malaysia. *Mar. Pollut. Bull.* **2018**, *136*, 135–140.
- (21) Nadiratuzzahra, S.; Tristantini, D. Cellulose acetate from oil palm empty fruit bunches waste as biodegradable microbeads for making scrubs. *AIP Conf. Proc.* **2020**, 2223, 050001.
- (22) Lochhead, R. Y. *Cosmetic science and technology: Theoretical principles and applications*; 2017; Chapter 13: The use of polymers in cosmetic products, pp 171–221.
- (23) Draelos, Z. D. Cosmetic Formulation of Skin Care Products; CRC Press, 2005; pp 25–26.
- (24) Paul, S.; Dutta, A. Challenges and opportunities of lignocellulosic biomass for anaerobic digestion. *Resour. Conserv. Recy.* **2018**, *130*, 164–174.

- (25) Standard Test Method for Determining Anaerobic Biodegradation of Plastic Materials Under Accelerated Landfill Conditions. *ASTM* **2018**, Standard D5526.
- (26) Tian, W.; Gao, X.; Zhang, J.; Yu, J.; Zhang, J. Cellulose nanosphere: Preparation and applications of the novel nanocellulose. *Carbohydr. Polym.* **2022**, 277, 118863.
- (27) Wang, H.; Zuo, M.; Ding, N.; Yan, G.; Zeng, X.; Tang, X.; Sun, Y.; Lei, T.; Lin, L. Preparation of Nanocellulose with High-Pressure Homogenization from Pretreated Biomass with Cooking with Active Oxygen and Solid Alkali. *ACS Sustain. Chem. Eng.* **2019**, *7*, 9378–9386.
- (28) Al Hakkak, J.; Grigsby, W. J.; Kathirgamanathan, K.; Edmonds, N. R. Generation of spherical cellulose nanoparticles from ionic liquid processing via novel nonsolvent addition and drying. *Adv. Mater. Sci. Eng.* **2019**, *2019*.
- (29) Beisl, S.; Miltner, A.; Friedl, A. Lignin from micro-to nanosize: production methods. *Int. J. Mol. Sci.* **2017**, *18*, 1244.
- (30) Tian, D.; Guo, Y.; Huang, M.; Zhao, L.; Deng, S.; Deng, O.; Zhou, W.; Hu, J.; Shen, F. Bacterial cellulose/lignin nanoparticles composite films with retarded biodegradability. *Carbohydr. Polym.* **2021**, *274*, 118656.
- (31) Ge, Y.; Qin, L.; Li, Z. Lignin microspheres: An effective and recyclable natural polymer-based adsorbent for lead ion removal. *Mater. Des.* **2016**, *95*, 141–147.
- (32) Hamdi, G.; Ponchel, G. Enzymatic Degradation of Epichlorohydrin Crosslinked Starch Microspheres by α -Amylase. *Pharm. Res.* **1999**, *16*, 867–875.
- (33) Puls, J.; Wilson, S. A.; Hölter, D. Degradation of Cellulose Acetate-Based Materials: A Review. *J. Polym. Environ.* **2011**, *19*, 152–165.
- (34) Vella, K. *Biodegradability of plastics in the open environment*; Science Advice for Policy by European Academies (SAPEA) Berlin, Germany, 2019.

- (35) King, C. A.; Shamshina, J. L.; Zavgorodnya, O.; Cutfield, T.; Block, L. E.; Rogers, R. D. Porous chitin microbeads for more sustainable cosmetics. *ACS Sustain. Chem. Eng.* **2017**, *5*, 11660–11667.
- (36) Alvarez, F. J. The Effect of Chitin Size, Shape, Source and Purification Method on Immune Recognition. *Molecules* **2014**, *19*, 4433–4451.
- (37) L. Shamshina, J. Chitin in ionic liquids: historical insights into the polymer's dissolution and isolation. A review. *Green Chem.* **2019**, *21*, 3974–3993.
- (38) Poncelet, D.; Lencki, R.; Beaulieu, C.; Halle, J. P.; Neufeld, R. J.; Fournier, A. Production of alginate beads by emulsification/internal gelation. I. Methodology. *Appl. Microbiol. Biotechnol.* **1992**, *38*, 39–45.
- (39) Chan, E.-S.; Lim, T.-K.; Voo, W.-P.; Pogaku, R.; Tey, B. T.; Zhang, Z. Effect of formulation of alginate beads on their mechanical behavior and stiffness. *Particuology* **2011**, *9*, 228–234.
- (40) Utomo, N. W.; Nazari, B.; Parisi, D.; Colby, R. H. Determination of intrinsic viscosity of native cellulose solutions in ionic liquids. *J. Rheol.* **2020**, *64*, 1063–1073.
- (41) Owens, C. E.; Du, J.; Sánchez, P. B. Understanding the Dynamics of Cellulose Dissolved in an Ionic Liquid Solvent Under Shear and Extensional Flows. *Biomacromolecules* **2022**, *23*, 1958–1969.
- (42) Robertson, B.; Hoover, L.; Rott, G.; Quan, M.; Calabrese, M. Development of microbeads from unmodified biomass with tunable size and competitive mechanical properties. *Cellulose* **2023**, *30*, 8839–8859.
- (43) Jenjob, R.; Phakkeeree, T.; Seidi, F.; Theerasilp, M.; Crespy, D. Emulsion Techniques for the Production of Pharmacological Nanoparticles. *Macromol. Biosci.* **2019**, *19*, 1900063.
- (44) Jo, S.; Park, S.; Oh, Y.; Hong, J.; Kim, H. J.; Kim, K. J.; Oh, K. K.; Lee, S. H. Development

- of Cellulose Hydrogel Microspheres for Lipase Immobilization. *Biotechnol. Bioproc. Eng.* **2019**, *24*, 145–154.
- (45) Park, S.; Oh, Y.; Yun, J.; Yoo, E.; Jung, D.; Oh, K. K.; Lee, S. H. Cellulose/biopolymer/Fe3O4 hydrogel microbeads for dye and protein adsorption. *Cellulose* **2020**, *27*, 2757–2773.
- (46) Daerr, A.; Mogne, A. Pendent_Drop: An ImageJ Plugin to Measure the Surface Tension from an Image of a Pendent Drop. *J. Open Res. Softw.* **2016**, *4*, e3.
- (47) Robertson, B. P.; Calabrese, M. A. Evaporation-controlled dripping-onto-substrate (DoS) extensional rheology of viscoelastic polymer solutions. *Sci. Rep.* **2022**, *12*, 4697.
- (48) Lauser, K. T.; Rueter, A. L.; Calabrese, M. A. Small-volume extensional rheology of concentrated protein and protein-excipient solutions. *Soft Matter* **2021**, *17*, 9624–9635.
- (49) Johnson, K. L.; Kendall, K.; Roberts, A. D.; Tabor, D. Surface energy and the contact of elastic solids. *Proc. R. Soc. Lond. Ser. A* **1997**, *324*, 301–313.
- (50) A. Tiba, A.; A. Perman, J.; R. MacGillivray, L.; V. Tivanski, A. Supramolecular modification of a metal–organic framework increases sorption switching: insights into reversible structural deformation of ZIF-8. *J. Mater. Chem. A.* **2022**, *10*, 21053–21060.
- (51) Chinga, G.; Johnsen, P. O.; Dougherty, R.; Berli, E. L.; Walter, J. Quantification of the 3D microstructure of SC surfaces. *J. Microsc.* **2007**, 227, 254–265.
- (52) Kumar, S.; Ganvir, V.; Satyanand, C.; Kumar, R.; Gandhi, K. S. Alternative mechanisms of drop breakup in stirred vessels. *Chem. Eng. Sci.* **1998**, *53*, 3269–3280.
- (53) DeBons, F. E.; Whittington, L. E. Improved oil recovery surfactants based on lignin. *J. Pet. Sci. Eng.* **1992**, *7*, 131–138.
- (54) Evdokimov, A. N.; Kurzin, A. V.; Fedorova, O. V.; Lukanin, P. V.; Kazakov, V. G.; Trifonova, A. D. Desulfurization of kraft lignin. *Wood Sci. Technol.* **2018**, *52*, 1165–1174.

- (55) Zaheer, Z.; AL-Asfar, A.; Aazam, E. S. Adsorption of methyl red on biogenic Ag@Fe nanocomposite adsorbent: Isotherms, kinetics and mechanisms. J. Mol. Liq. 2019, 283, 287–298.
- (56) Shah, A.-u.-H. A.; Ali, K.; Bilal, S. Surface tension, surface excess concentration, enthalpy and entropy of surface formation of aqueous salt solutions. *Colloid Surf. A: Physicochem. Eng. Asp.* **2013**, *417*, 183–190.
- (57) Pegram, L. M.; Record, M. T. Hofmeister Salt Effects on Surface Tension Arise from Partitioning of Anions and Cations between Bulk Water and the Air-Water Interface. *J. Phys. Chem. B* 2007, 111, 5411–5417.
- (58) Miller, A. F.; Donald, A. M. Surface and Interfacial Tension of Cellulose Suspensions. *Lang-muir* **2002**, *18*, 10155–10162.
- (59) Schuermann, J.; Huber, T.; LeCorre, D.; Mortha, G.; Sellier, M.; Duchemin, B.; Staiger, M. P. Surface tension of concentrated cellulose solutions in 1-ethyl-3-methylimidazolium acetate. *Cellulose* **2016**, *23*, 1043–1050.
- (60) McKinley, G. H. Visco-elasto-capillary thinning and break-up of complex fluids. *Rheology Reviews* **2005**, *05-P-04*, 1–50.
- (61) Figueiredo, R. A.; Oishi, C. M.; Afonso, A. M.; Alves, M. A. Numerical study on micro-scale extensional viscoelastic flows. *J. Non-Newton. Fluid Mech.* **2020**, *276*, 104219.
- (62) Sousa, P. C.; Vega, E. J.; Sousa, R. G.; Montanero, J. M.; Alves, M. A. Measurement of relaxation times in extensional flow of weakly viscoelastic polymer solutions. *Rheol. Acta* 2017, 56, 11–20.
- (63) Verbeke, K.; Formenti, S.; Vangosa, F. B.; Mitrias, C.; Reddy, N. K.; Anderson, P. D.; Clasen, C. Liquid bridge length scale based nondimensional groups for mapping transitions between regimes in capillary break-up experiments. *Phys. Rev. Fluids* **2020**, *5*, 051901.

- (64) Mecherbet, A. On the sedimentation of a droplet in Stokes flow. *Commun. Math. Sci.* **2021**, *19*, 1627—1654.
- (65) Ilyin, S. O.; Kostyuk, A. V.; Anokhina, T. S.; Melekhina, V. Y.; Bakhtin, D. S.; Antonov, S. V.; Volkov, A. V. The Effect of Non-Solvent Nature on the Rheological Properties of Cellulose Solution in Diluted Ionic Liquid and Performance of Nanofiltration Membranes. *Int. J. Mol. Sci.* 2023, 24, 8057.
- (66) Omura, T.; Suzuki, T.; Minami, H. Preparation of Cellulose Particles with a Hollow Structure. *Langmuir* **2020**, *36*, 14076–14082.
- (67) Torza, S.; Mason, S. G. Three-phase interactions in shear and electrical fields. *J. Colloid Interface Sci.* **1970**, *33*, 67–83.
- (68) Johnson, R. E.; Sadhal, S. S. Fluid Mechanics of Compound Multiphase Drops and Bubbles. *Annu. Rev. Fluid Mech.* **1985**, *17*, 289–320.
- (69) Grace, H. P. Dispersion phenomena in high viscosity immiscible fluid systems and application of static mixers as dispersion devices in such systems. *Chem. Eng. Commun.* **1982**, *14*, 225–277.
- (70) Bentley, B. J.; Leal, L. G. An experimental investigation of drop deformation and breakup in steady, two-dimensional linear flows. *J. Fluid Mech.* **1986**, *167*, 241–283.

TOC Graphic

